Journal of Materials Chemistry A

Carbon Nanotubes to Outperform Metal Electrodes in Perovskite Solar Cells via Dopant Engineering and Hole-Selectivity Enhancement

Journal:	*Journal of Materials Chemistry A*
Manuscript ID	TA-COM-04-2020-003692.R1
Article Type:	Communication
Date Submitted by the Author:	13-May-2020
Complete List of Authors:	Jeon, Il; The University of Tokyo, Shawky, Ahmed; The University of Tokyo - Hongo Campus, Mechanical Engineering; Central Metallurgical Research and Development Institute, Nanomaterials and Nanotechnology Seo, Seungju; The University of Tokyo - Hongo Campus, Mechanical Engineering Qian, Yang; The University of Tokyo - Hongo Campus, Mechanical Engineering Anisimov, Anton; Canatu Ltd., Kauppinen, Esko; Aalto University, Applied Physics Matsuo, Yutaka; The University of Tokyo, Department of Mechanical Engineering; University of Science and Technology of China, Hefei National Laboratory for Physical Sciences at the Microscale Maruyama, Shigeo; The University of Tokyo - Hongo Campus, Mechanical Engineering

Journal Name

COMMUNICATION

Carbon Nanotubes to Outperform Metal Electrodes in Perovskite Solar Cells via Dopant Engineering and Hole-Selectivity Enhancement

Received 00th January 20xx,
Accepted 00th January 20xx

DOI: 10.1039/x0xx00000x

www.rsc.org/

Il Jeon,*‡[ab] Ahmed Shawky,‡[ac] Seungju Seo,[a] Yang Qian,[a] Anton Anisimov,[d] Esko I. Kauppinen,[e] Yutaka Matsuo,*[a,f] Shigeo Maruyama*[a,g]

Triflic acid dispersed in an apolar solvent exhibited superior doping effect and stability on carbon nanotubes electrodes. By applying a high concentration of hole-transporting material to the carbon nanotube top electrode in perovskite solar cells, higher power conversion efficiency than the metal electrode-based perovskite solar cells was obtained.

Lead halide perovskite solar cells (PSCs) have received considerable attention around the world as a promising alternative energy source.[1] Their certified power conversion efficiencies (PCEs) now exceed 20% and only a few challenges remain before commercialisation,[2] which include long-term device stability and fabrication-cost.[3,4] In general, PSCs have a structure in which a photoactive material and two charge-selective materials are sandwiched by a transparent bottom electrode and a metal top electrode. The metal electrodes are typically evaporated in vacuum by thermal deposition. This incurs substantial fabrication costs.[5,6] Further, the metal electrodes induce metal-ion migration, which accelerates the degradation of perovskite layers.[7] Therefore, it is crucial that we find an alternative to the metal electrodes to maximise the low-cost merit of PSCs and remedy the shortcoming of poor device stability.

Having high conductivity and low-cost processability, aerosol-synthesised single-walled carbon nanotubes (CNTs) have showcased the promising potential as the top electrodes in PSCs.[8–11] The CNT top electrodes improve the PSC stability by both removing the metal-ion migration[12] and forming an effective moisture barrier[13]. Furthermore, the fact that CNTs are made up of carbon atoms only[14] and the aerosol-synthesised CNT films are dry- and direct-transferable[15,16] significantly reduces the solar cell fabrication cost. Thus far, the only drawback of the CNT top electrodes in PSCs has been an inadequate PCE. There are two main reasons for this: the first reason is that CNT electrodes do not reflect the incident light for reabsorption, unlike the metal electrodes. Therefore, the total external quantum efficiency (EQE) is lower than that of the metal electrode-based PSCs, which results in lower short-circuit current (J_{SC}). The second reason is the limited conductivity of CNTs, which can be improved by chemical doping, but it is extremely challenging as applying any chemicals onto CNTs will damage the underlying perovskite layer. This limits fill factor (FF) and open-circuit voltage (V_{OC}) of the CNT-based PSCs. Recently, we reported a vapour-assisted ex-situ doping method, which can effectively dope CNT top electrodes without damaging the layers underneath.[17] A PCE of 17.56% was obtained, which was the highest PCE among the CNT top electrode-based PSCs reported to date. However, this method has a problem of its own as the long exposure to acid vapour results in a reaction between the acidic dopant and 4-tert-butylpyridine (*t*-BP), limiting the doping effectiveness. Moreover, it is difficult to control the exposure time precisely, resulting in low reproducibility. Therefore, it is necessary to develop a more controlled and effective doping method that can be applied to the CNT top electrodes without damaging the neighbouring layers. In addition to this, for the CNT electrodes to outperform the metal electrodes, there has to be a way that is unique to CNTs which can improve the device performance even higher, other than *p*-doping. Herein, we report CNT electrode-laminated PSCs (CNT-PSCs), in which triflic acid (TFMS) dispersed in a non-polar solvent is cast onto the CNT top electrodes. This induces a stable doping effect without damaging the underneath perovskite layer as well as avoiding

---

[a] Department of Mechanical Engineering, The University of Tokyo 7-3-1 Hongo, Bunkyo-ku, Tokyo 113-8656, Japan.
[b] Department of Chemistry Education, Graduate School of Chemical Materials, Institute for Plastic Information and Energy Materials, Pusan National University, 63-2 Busandaehak-ro, Busan 46241, South Korea.
[c] Nanomaterials and Nanotechnology Department, Advanced Materials Division, Central Metallurgical R&D Institute (CMRDI), P.O. Box 87 Helwan, Cairo 11421, Egypt
[d] Canatu, Ltd., Konalankuja 5, FI-00390 Helsinki, Finland
[e] Department of Applied Physics, Aalto University School of Science, P.O. Box 15100, FI-00076 Aalto, Espoo, Finland
[f] Institute of Materials Innovation, Institutes of Innovation for Future Society, Nagoya University, Furo-cho, Chikusa-ku, Nagoya 464-8603, Japan
[g] Energy NanoEngineering Lab., National Institute of Advanced Industrial Science and Technology (AIST), Tsukuba, 305-8564, Japan

Electronic Supplementary Information (ESI) available: [details of any supplementary

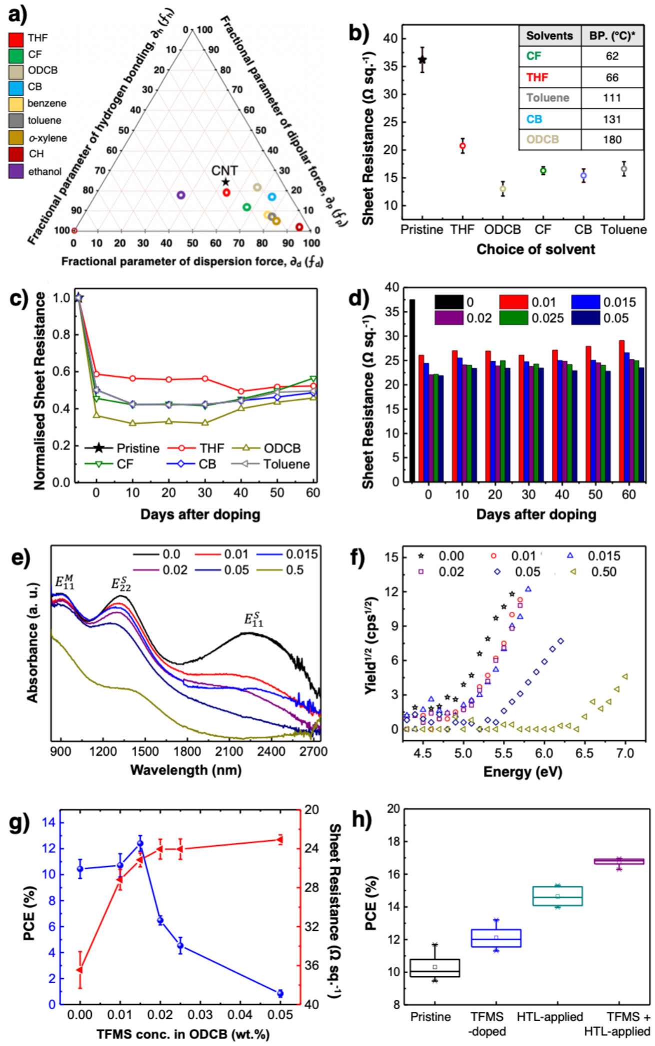

Fig. 1 a) Teas plot of the Hansen solubility parameters of CNT (black), THF (red), CF (green), ODCB (silver), CB (turquoise), benzene (magenta), toluene (grey), *o*-xylene (gold), CH (magenta) and ethanol (purple). b) sheet resistance change of a CNT film upon TFMS doping by different solvents and the boiling points of those solvents in the inset. c) Normalised sheet resistance change of the CNT films doped by TFMS in different solvents over 60 days in air. d) sheet resistance change of CNT films doped by TFMS in different concentration of ODCB. e) Vis-NIR spectra of the CNT films doped by TFMS in different concentration of ODCB. f) PYS measurements of the CNT films doped by TFMS in different concentration of ODCB. g) PCE (blue circles) and the corresponding sheet resistance (red triangles) of the TFMS-doped CNT in CNT-based PSCs over different concentrations of TFMS in ODCB. h) PCE of CNT-laminated PSCs (black), TFMS-doped CNT-laminated PSCs (blue), HTL-applied CNT-laminated PSCs (green) and HTL-applied TFMS-doped CNT-laminated PSCs (purple).

reaction with t-BP. We found that the dispersion force, polarity force, and hydrogen force of the solvents are directly related to the doping effectiveness in CNTs. Based on this, o-dichlorobenzene (ODCB) solvent for TFMS was found to exhibit the greatest doping effect and 0.015 wt.% of TFMS was the optimal concentration that showed the maximum doping effect with the minimum damage to the device system. To improve the PCE further, we optimised the 2,2′,7,7′-tetrakis(N,N-di-p-methoxyphenylamine)-9,9′-spirobi-fluorene (spiro-MeOTAD) concentration and the CNT film density. It is well known that amorphous spiro-MeOTAD has relatively low mobility, thus the thickness of the spiro-MeOTAD layer cannot exceed certain point.[18,19] Harnessing the unique geometry of the porous CNT network, we found that the CNT films can accommodate a greater concentration of spiro-MeOTAD without lowering the hole-mobility. Besides, different CNT film densities possess different pore sizes within the CNT films for spiro-MeOTAD to accommodate. Upon optimizing both the concentration and the CNT density, a 1.17 times higher spiro-MeOTAD concentration with the 80% transparent (at the wavelength of 550 nm) CNT films led to the highest PCE of 18.8% in PSCs. Not only was this the record-high efficiency among the reported CNT top electrode-based PSCs, but this was also higher than that of the metal electrode-based control devices, which gave a PCE of 18.4%. This sets a milestone for the CNT-applied PSCs as this is the first time for carbon electrodes to outperform metal electrodes in pho photovoltaics to the best of our knowledge. Moreover, it is worth emphasizing that the CNT-PSCs demonstrated in this work are semi-transparent which have great potential for other applications, such as tandem solar cells.[20,21]

TFMS is a superacid with a Hammett acidity function (H_0) of approximately −14.9. TFMS is one of the most effective and durable dopants for carbon electrodes.[22,23] In our previous study, we used TFMS vapour to dope CNT top electrodes in CNT-PSCs.[17] However, this method resulted in TFMS molecules building up at the interface between the CNT electrode and the perovskite, reacting with t-BP (**Fig.S1a**). The presence of t-BP at the perovskite surface is crucial to PSC efficiency as they induce favourable chemical interactions[24] and improve the morphology[25] of the perovskite layers. Therefore, it is Ideal to use the drop-cast doping method in the viewpoints of reproducibility and doping effectiveness; the drop-casted TFMS solution will dope the CNT network more thoroughly and minimise the reaction with t-BP at the perovskite interface (**Fig. S1b**). However, drop-casting a polar solvent directly onto the CNT electrode will dissolve the perovskite layer underneath. Hence, we explored various non-polar solvents, namely tetrahydrofuran (THF), chloroform (CF), ODCB, chlorobenzene (CB), benzene, toluene, o-xylene, cyclohexane (CH), and ethanol to disperse TFMS for the drop-cast doping (**Fig. S2**). The influence of the solvents on the doping effect and stability was investigated. Non-ionic molecular interaction between CNTs and the solvent can be predicted by Hansen parameters, namely, dispersion force, (f_d) polar force (f_p), and hydrogen bonding force (f_h).[26,27] These three-component data can be translated onto a triangular graph, known as the Teas plot (1)(2).

$$\begin{aligned} f_d &= \partial_d/\partial_d + \partial_p + \partial_h \\ f_p &= \partial_p/\partial_d + \partial_p + \partial_h \\ f_h &= \partial_h/\partial_d + \partial_p + \partial_h \end{aligned} \qquad (1)$$

$$f_d + f_p + f_h = 100 \qquad (2)$$

Fig. 1a shows a Teas plot depicting compatibility between CNT and different solvents. It can be said that the distance of a

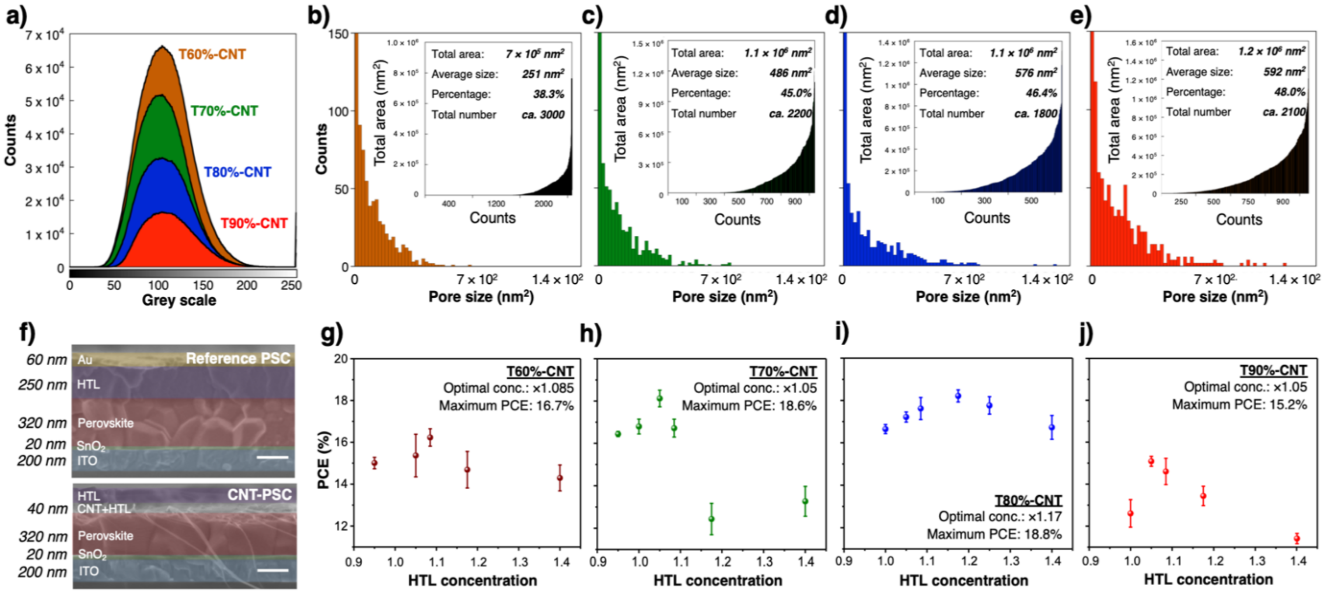

Fig. 2 a) The image contrast histogram of the unprocessed SEM images of CNT films with different densities. Image analysis of b) T60%-CNT, c) T70%-CNT, d) T80%-CNT and e) T90%-CNT. f) Cross-sectional SEM images of metal electrode-based PSCs and CNT-based PSCs. PCEs of CNT-based PSCs with different spiro-MeOTAD concentrations for g) T60%-CNT, h) T70%-CNT, i) T80%-CNT and j) T90%-CNT.

solvent from the CNT on the Teas plot represents how thoroughly TFMS permeates into the CNT network. The sheet resistance change of the CNT films upon TFMS doping (conc. 0.5 wt.%) measured by the Van der Pauw method (**Fig. S3**) shows that while the effectiveness of the doping generally follows the Teas plot, some discrepancies are present due probably to varying vapour pressures of the solvents (**Fig. 1b**). Ideally, solvents which pervade into the CNTs without evaporating too quickly are expected to induce the greatest doping effect. **Fig. 1b** shows that TFMS in ODCB displays the greatest doping effect as the sheet resistance dropped from *ca.* 36 Ω sq.$^{-1}$ to *ca.* 13 Ω sq.$^{-1}$. ODCB sits rather close to that of CNT on the teas plot and has a relatively high boiling point. It is an interesting finding that acids do not need to be dissolved in order to induce strong doping. The doping durability of TFMS in different solvents was also measured. All of the solvents showed longer than 30 days of doping durability in air, corroborating that the choice of solvents does not affect the durability of the doping effect (**Fig. 1c, Fig. S4**). In order to minimise the potential damage caused by TFMS, we tested low concentrations of TFMS dispersed in ODCB. Even a small concentration as low as 0.01 wt.% induced a significant doping effect and the concentration of the acid did not affect the doping durability (**Fig. 1d**). The doping effect was confirmed by the (Vis-NIR) visible to near infra-red absorption spectroscopy, photoelectron yield spectroscopy (PYS) and Raman spectroscopy. The suppression of the van Hove singularity transitions (E^M_{11}, E^S_{22}, and E^S_{11}) in **Fig. 1e** and lowering of the Fermi level in **Fig. 1f** reveal that even 0.01 wt.% TFMS induces substantial *p*-doping.[28,29] Additionally, the suppressed radial breathing mode (RBM) of the Raman spectrum (**Fig. S5a**)[30–33] and the G-band shift by 1.6 cm^{-1} upon application of 0.01 wt.% TFMS to a CNT film confirms the doping (**Fig. S5b**).[22,34,35] It is worth noting that there are reductions in the D-band to G-band intensity ratio (I_D/I_G) from 0.016 to 0.012 (**Fig. S5c**).[36] While *p*-doping by a low concentration of acid has been reported to decrease I_D/I_G,[31,33,37] it may simply be due to removal of impurities on CNTs by acid[38]. Whichever the reason may be, it is clear that even the trace amount of TFMS has a considerable effect on CNTs. To assess the doping effect in devices, CNT-PSCs were fabricated in a configuration of glass/indium tin oxide (ITO)/SnO_2/$CH_3NH_3PbI_3$ ($MAPbI_3$)/CNT. Different concentrations of TFMS in ODCB were applied to the top CNT electrode and 0.015 wt.% TFMS gave the highest photovoltaic performance (**Fig. 1g, Table S1**). Increasing the TFMS concentration decreased the PCE of the CNT-PSCs. We ascribe this to the proton migration[39–41] and the hygroscopic nature of TFMS[17] degrading the perovskite layer (**Fig. S6**). X-ray diffraction (XRD) measurement shows that the application of TFMS acid leads to the breakdown of $MAPbI_3$ into intermediates, indicated by the increase in the PbI_2 peak and the appearance of the intermediate peaks (**Fig. S7**).[42,43] Having found the optimal concentration of TFMS, we applied the spiro-MeOTAD hole-transporting layer (HTL) to boost the PCE. **Fig. 1h** shows that spin-coating spiro-MeOTAD HTL on top of the TFMS-doped CNT-PSCs increased the PCE from 13.2% To 17.0% (**Fig. S8, Table S2**).

It is evident that the reaction between TFMS and t-BP is minimal if at all. The application of TFMS and HTL enhanced all three parameters. TMFS doping improved FF by decreasing the series resistance (R_S) and HTL application improved FF by increasing the shunt resistance (R_{SH}) (**Fig. S9**). TFMS doping increased V_{OC} as well by improving the energy alignment between the Fermi level of the CNT electrode and the valence level of the perovskite layer as evidenced by photoluminescent (PL) quenching (**Fig. S10**).[17,44]
While the PCE of 17.0% from the $MAPbI_3$-based CNT-PSC is already a high value, there is room for further improvement. The density of CNT films can be controlled by the aerosol CNT

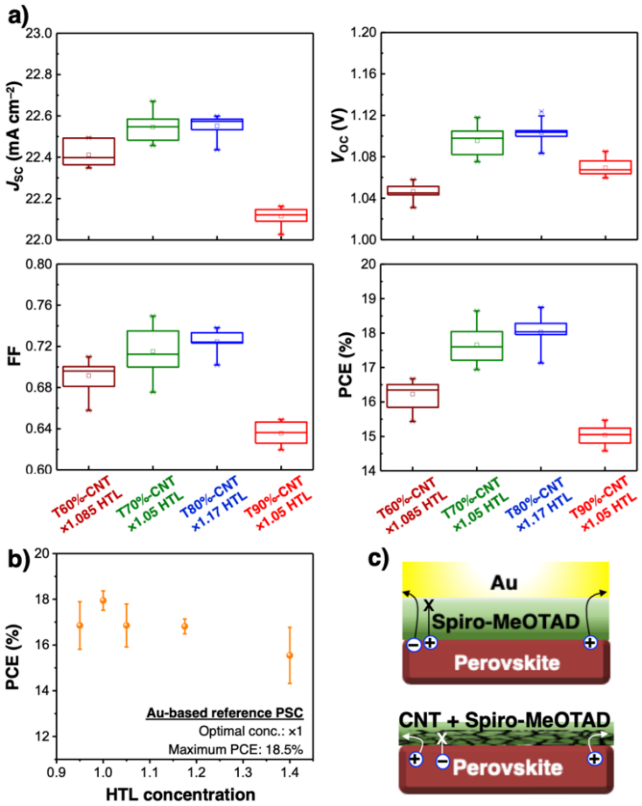

Fig. 3 a) Photovoltaic parameters of the CNT-based PSCs with the optimum spiro-MeOTAD concentration. b) The metal electrode-based PSCs with different spiro-MeOTAD concentrations. c) Depiction of the charge flow in a metal-based PSC (above) and a CNT-based PSC (below).

collection time. The longer collection time, the denser CNT film. There is a trade-off between the transparency and conductivity of the CNT films according to their collection time (**Fig. S11, Table S3**).[11,15] When CNT films are used as the top electrode, the transparency is not important. However, we cannot merely employ CNT films with the highest density. This is because CNT films with different density have a different pore size, which can accommodate different amounts of spiro-MeOTAD. Therefore, using CNT films with the highest density limits the hole-transporting ability as they accommodate small amount spiro-MeOTAD. We analysed the scanning electron microscopic (SEM) images of the CNT films with four different densities (indicated by their transparency, T at a wavelength of 550 nm), *viz.* T90%-CNT, T80%-CNT, T70%-CNT and T60%-CNT (**Fig. S12**). The image contrast histogram of the unprocessed SEM images shows that there are more grey images for the denser CNT films, reflecting a greater number of tubes (**Fig. 2a**). By processing the SEM images, we obtained information regarding the number and size of the pores within the CNT network (**Fig. 2 b-e, Fig. S13**). The data show that the densest, T60%-CNT films have the smallest pore size (**Fig. 2b**). While the number and size of the pores among T70%-CNT, T80%-CNT, and T90%-CNT were similar, T90%-CNT films had some conspicuously large pores (**Fig. S14**). This meant that we had to test different concentrations of spiro-MeOTAD HTL for CNT-PSCs. Au electrode-based reference PSCs and CNT-PSCs were fabricated using different HTL concentration (**Fig. 2f**). While both the T60%-CNT- and the T90%-CNT-based PSCs gave low PCEs, the T70%-CNT- and the T80%-CNT-based PSCs exhibited the highest PCEs of 18.6% and 18.8%, respectively (**Fig. 2 g-j**). The optimal HTL concentrations were 1.05 and 1.17 times higher than the commonly used spiro-MeOTAD concentration used the Au-based PSCs.

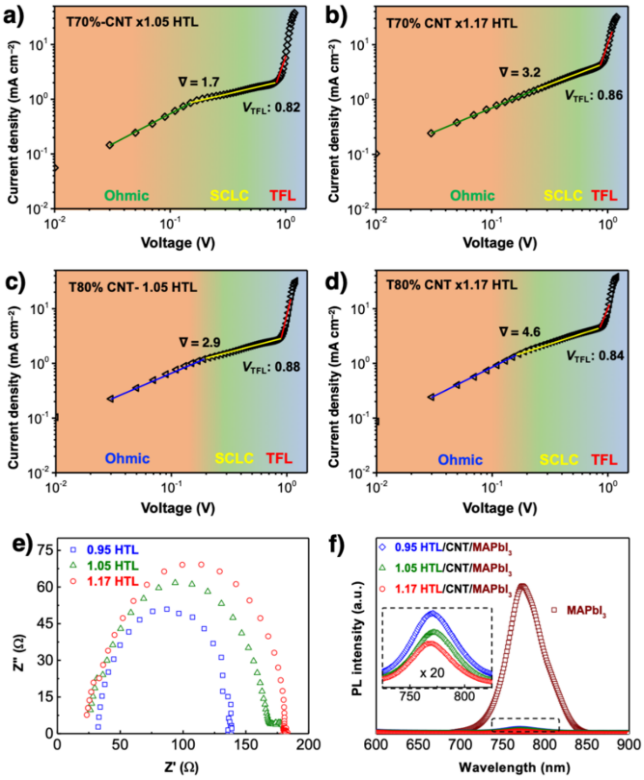

Fig. 4 SCLC measurement of a) T70%-CNT with x1.05 HTL-applied hole-only device, b) T70%-CNT with x1.17 HTL-applied hole-only device, c) T80%-CNT with x1.05 HTL-applied hole-only device and d) T80%-CNT with x1.17 HTL-applied hole-only device. e) EIS data of T80%-CNT-PSCs with x0.95 (blue square), x1.05 (green triangle) and x1.17 (red circles) HTL concentrations. f) PL of a perovskite film (brown), x0.95 HTL-applied CNT (blue), x1.05 HTL-applied CNT (green) and x1.05 HTL-applied CNT (red) on the perovskite film with the x20 magnification in the inset.

By looking at the photovoltaic parameters of the HTL-optimised CNT-based PSCs, it is clear that the high PCE arises from high J_{SC} and FF, which are related to the charge extraction and hole-selectivity, respectively (**Fig. 3a**). In the case of conventional metal electrode-based PSCs, increasing the spiro-MeOTAD HTL concentration decreased the PCE (**Fig. 3b**). This is because increasing the HTL concentration results in a thicker spiro-MeOTAD layer, which leads to a decrease in the hole-transporting ability as verified by the increase in R_S (**Fig. S15, Table S4**). Decreasing the spiro-MeOTAD concentration led to the increased hole-transporting ability, yet the electron-blocking ability decreases as verified by the decrease in R_{SH} (**Fig. S16, Table S5**). This does not happen in the case of the CNT-laminated PSCs because the thick layer of the spiro-MeOTAD layer is tolerated more on account of the hole being extracted by the CNT at the interface before being hindered by the limited hole mobility of spiro-MeOTAD (**Fig. 3c**). To verify this point, we carried out space-charge limited current (SCLC) measurement on CNT-laminated hole-only devices (ITO/poly(3,4-

ethylenedioxythiophene) polystyrene sulfonate (PEDOT:PSS)/MAPbI$_3$/CNT/spiro-MeOTAD) with two different CNT densities and three different concentrations of spiro-MeOTAD. The hole mobility (μ) is correlated to the gradient of the current to voltage in the SCLC region (▽) (3). The charge trap density (n_{trap}) is correlated to the trap-filled limit voltage (V_{TFL}), which is the beginning point of the TFL region (4).

$$J = 9/8 \times \mathcal{E}_0\mathcal{E}_r\mu(V^2/\,L^3) \;\rightarrow \mu \propto k(J/V^2) \qquad (3)$$

$$n_{trap} = 2\mathcal{E}_r V_{TFL}/qL^2 \;\rightarrow\; n_{trap} \propto kV_{TFL} \qquad (4)$$

The SCLC curve gradients in **Fig. 4a**, **4b**, **4c** and **4d** show that the hole-mobility increases with the increase in the HTL concentration, and the increase is greater for the T80%-CNT than the T70%-CNT. V_{TFL} values are lower for the 1.05 times concentrated HTL-applied T70%-CNT than the 1.17 times concentrated HTL-applied T70%-CNT, whereas the 1.17 times concentrated HTL-applied T80%-CNT exhibit less V_{TFL} than the 1.05 times concentrated HTL-applied T80%-CNT. This shows that both hole-mobility and n_{trap} indicate the hole-transporting efficiency of the CNT-PSCs. Electrochemical impedance spectroscopy (EIS) data of the different concentration of HTL-applied T80% CNT-based PSCs in **Fig. 4e** confirm that the increase in the HTL concentration increases the charge transport resistance (R_{CT}), which implies the electron-blocking ability enhancement as well as the hole mobility reduction (**Table S6**). Nevertheless, the photoluminescence (PL) quenching of different concentration of HTL-applied T80% CNT on perovskite films reveal that applying 1.17 times higher spiro-MeOTAD concentration to the T80% CNT film induces improved charge transfer as evidenced by the stronger quenching with a slight blue-shift, which indicates reduced charge trap sites (**Fig. 4f**).[45,46]

Combination of the optimised CNT density and spiro-MeOTAD concentration in CNT-PSCs gave the highest PCE of 18.8% and an average PCE of 18.3% (**Figure 5a** and **5b**, **Table 1**: entry 6, **Figure S17**), which are higher than 18.4% for the best PCE and 17.9% for the average PCE of the Au electrode-based reference PSCs (**Table 1**: entry 1). Such outperformance of the CNT-PSCs over the Au-based PSCs comes from the higher FF, which is attributed to the superior charge selectivity of the optimised spiro-MeOTAD concentration and CNT density along with the improved conductivity by the *p*-dopant solvent engineering (**Figure 5c**). Despite the lower J_{SC} coming from the non-reflective nature of the CNT top electrode, V_{OC} of the CNT-PSCs was equal or higher than that of the reference devices. This is ascribed to the better-aligned energy level between the CNT Fermi level and the valence band of MAPbI$_3$ as well as the reduced Shockley-Read-Hall recombination V_{OC} loss through more effective hole-extraction by the CNTs.[46,47] The obtained PCE of 18.8% stands the highest amongst the reported CNT electrode-based PSCs (**Figure 5d**, **Table S7**, **Figure S18, S19,** and **S20, S21**).[12,13,17,29,42,47–57] As reported many times before, the CNT-laminated PSCs' device stability was greater than that of the gold electrode-based PSCs (**Figure S22**). However, the

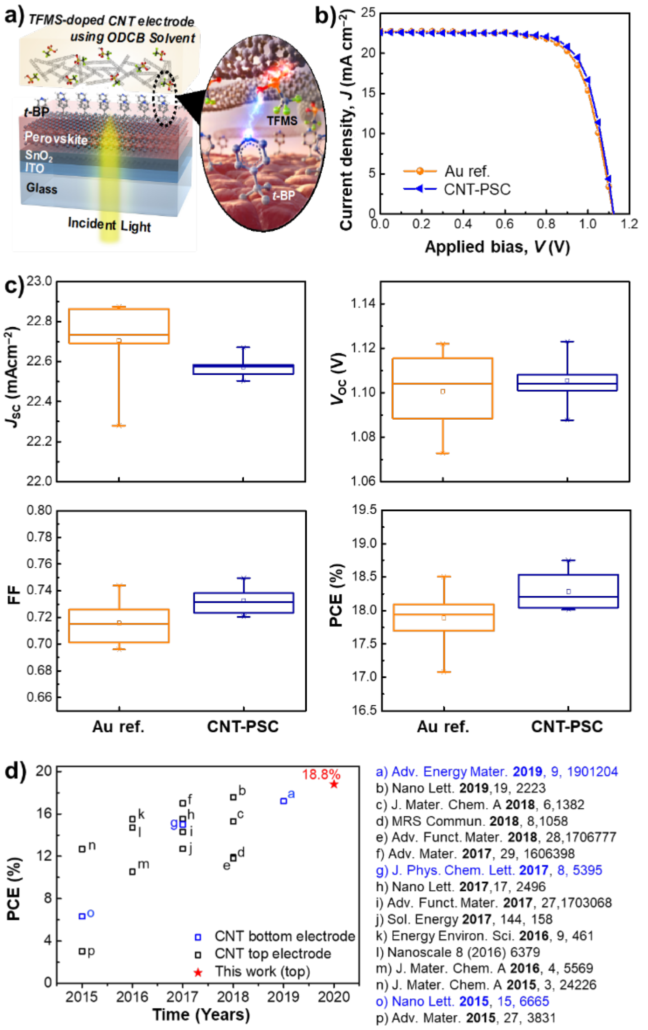

Fig. 5 a) Schematic representation of the optimised TFMS-doped CNT electrode PSC device. b) *J–V* curves of the Au-based PSC (orange circle) and the optimised TFMS-doped CNT-PSC (blue triangle). c) statistical analyses of the photovoltaic parameters of the two types of devices collected from the best 10 devices each. d) A chart showing record-high PCEs of all the CNT electrode-based PSCs reported this far.

Table 1. Photovoltaic parameters of the PSCs with gold electrode, CNT, TFMS-doped CNT, HTL-applied CNT, HTL-applied TFMS-doped CNT and optimized HTL-applied TFMS-doped CNT under 1 sun (AM 1.5 G, 100 mW cm^{-2}).

Entry	Top Electrode	J_{SC} (mA cm^{-2})	V_{OC} (V)	FF	PCE$_{Best}$ (%)	PCE$_{average}$ (%)
1	**Au**	**22.8**	**1.12**	**0.721**	**18.4**	**17.9 ±0.42**
2	CNT	19.8	0.97	0.595	11.4	10.4 ±0.72
3	TFMS-doped CNT	20.6	1.03	0.620	13.2	12.4 ±0.65
4	HTL-applied CNT	21.7	1.04	0.680	15.3	14.8 ±0.53
5	HTL-applied TFMS-doped CNT	22.5	1.08	0.700	17.0	16.7 ±0.14
6	**Optimised HTL-applied TFMS-doped CNT**	**22.7**	**1.12**	**0.738**	**18.8**	**18.3 ±0.54**

difference was not great, which we attribute to the use of hygroscopic TFMS. Nevertheless, this work sets a new milestone as this is the first time a CNT electrode surpasses a metal electrode in terms of solar cell efficiency as far as we are concerned. We plan on improving CNT-PSC technology further by advancing the doping methodology and the HTL materials. We are positive that this work will deepen the understanding of the device application of CNT electrodes and inspire other solar cell scientists to move a step closer to the feasible PSCs.

Conclusions

As our previous approach of using ex-situ TFMS vapour doping method led to a limited PCE, it was essential to develop a new doping method that leads to the minimal interaction with *t*-BP while demonstrating the maximum doping effect. Direct drop-casting of TFMS dispersed in a non-polar solvent was, therefore, investigated in this work. TFMS in ODCB was found to manifest superior doping effect and excellent stability compared with other solvents. Furthermore, by exploiting the high mobility of the porous CNT network, a higher concentration of spiro-MeOTAD was applied to the TFMS-doped CNT-laminated PSCs after the CNT density optimisation. The resulting CNT top electrode-laminated metal electrode-free PSCs exhibited a PCE of 18.8%, which is higher than 18.4% of the metal electrode-based PSCs. This is a momentous finding as we carve our own path with the CNT electrodes and finally surpassed the metal electrode in device application.

Conflicts of interest

There are no conflicts to declare.

Notes and references

‡ These authors contributed equally. We gratefully acknowledge the Research and Education Consortium for Innovation of Advanced Integrated Science by Japan Science and Technology (JST) and Japan Society for the Promotion of Science JSPS KAKENHI Grant Numbers JP15H05760, JP16H02285, JP17K04970, JP17H06609, JP17F17364, JP18H05329, and JP19K15669. I.J. thanks Yashima Environment Technology Foundation for financial support. This work was supported by the National Research Foundation of Korea (NRF) grant funded by the Korea government Ministry of Science and ICT (MSIT) (No. NRF-2018R1A5A1025594).

1 M. A. Green, A. Ho-Baillie and H. J. Snaith, *Nat. Photonics*, 2014, **8**, 506–514.

2 E. H. Jung, N. J. Jeon, E. Y. Park, C. S. Moon, T. J. Shin, T.-Y. Yang, J. H. Noh and J. Seo, *Nature*, 2019, **567**, 511–515.

3 N.-G. Park, M. Grätzel, T. Miyasaka, K. Zhu and K. Emery, *Nat. Energy*, 2016, **1**, 16152.

4 L. Meng, J. You and Y. Yang, *Nat. Commun.*, 2018, **9**, 5265.

5 I. Jeon, S. Seo, Y. Sato, C. Delacou, A. Anisimov, K. Suenaga, E. I. Kauppinen, S. Maruyama and Y. Matsuo, *J. Phys. Chem. C*, 2017, **121**, 25743–25749.

6 Z. Song, C. L. McElvany, A. B. Phillips, I. Celik, P. W. Krantz, S. C. Watthage, G. K. Liyanage, D. Apul and M. J. Heben, *Energy Environ. Sci.*, 2017, **10**, 1297–1305.

7 K. Domanski, J.-P. Correa-Baena, N. Mine, M. K. Nazeeruddin, A. Abate, M. Saliba, W. Tress, A. Hagfeldt and M. Grätzel, *ACS Nano*, 2016, **10**, 6306–6314.

8 I. Jeon, R. Xiang, A. Shawky, Y. Matsuo and S. Maruyama, *Adv. Energy Mater.*, 2019, **9**, 1801312.

9 I. Jeon, Y. Matsuo and S. Maruyama, *Top. Curr. Chem.*, 2018, **376**, 4.

10 A. G. Nasibulin, A. Kaskela, K. Mustonen, A. S. Anisimov, V. Ruiz, S. Kivistö, S. Rackauskas, M. Y. Timmermans, M. Pudas, B. Aitchison, M. Kauppinen, D. P. Brown, O. G. Okhotnikov and E. I. Kauppinen, *ACS Nano*, 2011, **5**, 3214–3221.

11 A. Kaskela, A. G. Nasibulin, M. Y. Timmermans, B. Aitchison, A. Papadimitratos, Y. Tian, Z. Zhu, H. Jiang, D. P. Brown, A. Zakhidov and E. I. Kauppinen, *Nano Lett.*, 2010, **10**, 4349–4355.

12 K. Aitola, K. Domanski, J.-P. Correa-Baena, K. Sveinbjörnsson, M. Saliba, A. Abate, M. Grätzel, E. Kauppinen, E. M. J. Johansson, W. Tress, A. Hagfeldt and G. Boschloo, *Adv. Mater.*, 2017, **29**, 1606398.

13 N. Ahn, I. Jeon, J. Yoon, E. I. Kauppinen, Y. Matsuo, S. Maruyama and M. Choi, *J. Mater. Chem. A*, 2018, **6**, 1382–1389.

14 R. A. Z, Wu, Chen Z, Du X, Logan JM, Sippel J, Nikolou M, Kamaras K, Reynolds JR, Tanner DB, Hebard AF, *Science*, 2004, **305**, 1273–1276.

15 I. Jeon, K. Cui, T. Chiba, A. Anisimov, A. G. Nasibulin, E. I. Kauppinen, S. Maruyama and Y. Matsuo, *J. Am. Chem. Soc.*, 2015, **137**, 7982–7985.

16 Z. Li, S. A. Kulkarni, P. P. Boix, E. Shi, A. Cao, K. Fu, S. K. Batabyal, J. Zhang, Q. Xiong, L. H. Wong, N. Mathews and S. G. Mhaisalkar, *ACS Nano*, 2014, **8**, 6797–6804.

17 J.-W. Lee, I. Jeon, H.-S. Lin, S. Seo, T.-H. Han, A. Anisimov, E. I. Kauppinen, Y. Matsuo, S. Maruyama and Y. Yang, *Nano Lett.*, 2019, **19**, 2223–2230.

18 Z. Hawash, L. K. Ono and Y. Qi, *Adv. Mater. Interfaces*, 2018, **5**, 1700623.

19 I. Jeon, H. Ueno, S. Seo, K. Aitola, R. Nishikubo, A. Saeki, H. Okada, G. Boschloo, S. Maruyama and Y. Matsuo, *Angew. Chemie Int. Ed.*, 2018, **57**, 4607–4611.

20 J. Zheng, H. Mehrvarz, F.-J. Ma, C. F. J. Lau, M. A. Green, S. Huang and A. W. Y. Ho-Baillie, *ACS Energy Lett.*, 2018, **3**, 2299–2300.

21 T. Leijtens, K. A. Bush, R. Prasanna and M. D. McGehee, *Nat. Energy*, 2018, **3**, 828–838.

22 T.-H. Han, S.-J. Kwon, N. Li, H.-K. Seo, W. Xu, K. S. Kim and T.-W. Lee, *Angew. Chemie Int. Ed.*, 2016, **55**, 6197–6201.

23 I. Jeon, C. Delacou, H. Okada, G. E. Morse, T.-H. Han, Y. Sato, A. Anisimov, K. Suenaga, E. I. Kauppinen, S. Maruyama and Y. Matsuo, *J. Mater. Chem. A*, 2018, **6**, 14553–14559.

24 S. N. Habisreutinger, N. K. Noel, H. J. Snaith and R. J. Nicholas, *Adv. Energy Mater.*, 2017, **7**, 1601079.

25 S. Wang, M. Sina, P. Parikh, T. Uekert, B. Shahbazian, A. Devaraj and Y. S. Meng, *Nano Lett.*, 2016, **16**, 5594–5600.

26 S. D. Bergin, Z. Sun, D. Rickard, P. V Streich, J. P. Hamilton

and J. N. Coleman, *ACS Nano*, 2009, **3**, 2340–2350.

27 A. P. Tsapenko, A. E. Goldt, E. Shulga, Z. I. Popov, K. I. Maslakov, A. S. Anisimov, P. B. Sorokin and A. G. Nasibulin, *Carbon N. Y.*, 2018, **130**, 448–457.

28 K. Cui, Y. Qian, I. Jeon, A. Anisimov, Y. Matsuo, E. I. Kauppinen and S. Maruyama, *Adv. Energy Mater.*, 2017, **7**, 1700449.

29 I. Jeon, J. Yoon, N. Ahn, M. Atwa, C. Delacou, A. Anisimov, E. I. Kauppinen, M. Choi, S. Maruyama and Y. Matsuo, *J. Phys. Chem. Lett.*, 2017, **8**, 5395–5401.

30 I. Puchades, C. C. Lawlor, C. M. Schauerman, A. R. Bucossi, J. E. Rossi, N. D. Cox and B. J. Landi, *J. Mater. Chem. C*, 2015, **3**, 10256–10266.

31 H.-Z. Geng, K. K. Kim, C. Song, N. T. Xuyen, S. M. Kim, K. A. Park, D. S. Lee, K. H. An, Y. S. Lee, Y. Chang, Y. J. Lee, J. Y. Choi, A. Benayad and Y. H. Lee, *J. Mater. Chem.*, 2008, **18**, 1261.

32 J. Strauch, B. Anis and C. A. Kuntscher, *Phys. status solidi*, 2014, **251**, 2378–2383.

33 W. Zhou, J. Vavro, N. M. Nemes, J. E. Fischer, F. Borondics, K. Kamarás and D. B. Tanner, *Phys. Rev. B*, 2005, **71**, 205423.

34 Y. Miyata, K. Yanagi, Y. Maniwa and H. Kataura, *J. Phys. Chem. C*, 2008, **112**, 3591–3596.

35 S. M. Kim, K. K. Kim, Y. W. Jo, M. H. Park, S. J. Chae, D. L. Duong, C. W. Yang, J. Kong and Y. H. Lee, *ACS Nano*, 2011, **5**, 1236–1242.

36 L. Yu, C. Shearer and J. Shapter, *Chem. Rev.*, 2016, **116**, 13413–13453.

37 P.-A. Tsai, H.-Y. Kuo, W.-M. Chiu and J.-H. Wu, *J. Nanomater.*, 2013, **2013**, 937697.

38 K. A. Wepasnick, B. A. Smith, K. E. Schrote, H. K. Wilson, S. R. Diegelmann and D. H. Fairbrother, *Carbon*, 2011, **49**, 24–36.

39 J. A. Dawson, T. S. Attari, H. Chen, S. P. Emge, K. E. Johnston and M. S. Islam, *Energy Environ. Sci.*, 2018, **11**, 2993–3002.

40 D. A. Egger, L. Kronik and A. M. Rappe, *Angew. Chemie Int. Ed.*, 2015, **54**, 12437–12441.

41 C. Cardenas-Daw, T. Simon, J. K. Stolarczyk and J. Feldmann, *J. Am. Chem. Soc.*, 2017, **139**, 16462–16465.

42 X. Guo, C. McCleese, C. Kolodziej, A. C. S. Saima, Y. Zhao, C. Burda, *Dalton Trans.*, 2016, **45**, 3806–3813.

43 M. Long, T. Zhang, Y. Chai, C.-F. Ng, T. C. W. Mak, J. Xu, K. Yan, *Nat. Commun.*, 2016, **7**, 13503.

44 I. Jeon, J. Yoon, U. Kim, C. Lee, R. Xiang, A. Shawky, J. Xi, J. Byeon, H. M. Lee, M. Choi, S. Maruyama and Y. Matsuo, *Adv. Energy Mater.*, 2019, **9**, 1901204.

45 H.-S. Lin, I. Jeon, R. Xiang, S. Seo, J.-W. Lee, C. Li, A. Pal, S. Manzhos, M. S. Goorsky, Y. Yang, S. Maruyama and Y. Matsuo, *ACS Appl. Mater. Interfaces*, 2018, **10**, 39590–39598.

46 S. Seo, I. Jeon, R. Xiang, C. Lee, H. Zhang, T. Tanaka, J.-W. Lee, D. Suh, T. Ogamoto, R. Nishikubo, A. Saeki, S. Chiashi, J. Shiomi, H. Kataura, H. M. Lee, Y. Yang, Y. Matsuo and S. Maruyama, *J. Mater. Chem. A*, 2019, **7**, 12987–12992.

47 H. Do Kim, H. Ohkita, H. Benten and S. Ito, *Adv. Mater.*, 2016, **28**, 917–922.

48 S. N. Habisreutinger, N. K. Noel, B. W. Larson, O. G. Reid, J. L. Blackburn, *ACS Energy Lett.*, 2019, **4**, 1872–1879.

49 Q. Luo, H. Ma, Q. Hou, Y. Li, J. Ren, X. Dai, Z. Yao, Y. Zhou, L. Xiang, H. Du, H. He, N. Wang, K. Jiang, H. Lin, H. Zhang and Z. Guo, *Adv. Funct. Mater.*, 2018, **28**, 1706777.

50 T. Sakaguchi, I. Jeon, T. Chiba, A. Shawky, R. Xiang, S. Chiashi, E. I. Kauppinen, N.-G. Park, Y. Matsuo and S. Maruyama, *MRS Commun.*, 2018, **8**, 1058–1063.

51 X. Zheng, H. Chen, Q. Li, Y. Yang, Z. Wei, Y. Bai, Y. Qiu, D. Zhou, K. S. Wong and S. Yang, *Nano Lett.*, 2017, **17**, 2496–2505.

52 Q. Luo, H. Ma, F. Hao, Q. Hou, J. Ren, L. Wu, Z. Yao, Y. Zhou, N. Wang, K. Jiang, H. Lin and Z. Guo, *Adv. Funct. Mater.*, 2017, **27**, 1703068.

53 S. Liu, K. Cao, H. Li, J. Song, J. Han, Y. Shen and M. Wang, *Sol. Energy*, 2017, **144**, 158–165.

54 K. Aitola, K. Sveinbjörnsson, J.-P. Correa-Baena, A. Kaskela, A. Abate, Y. Tian, E. M. J. Johansson, M. Grätzel, E. I. Kauppinen, A. Hagfeldt and G. Boschloo, *Energy Environ. Sci.*, 2016, **9**, 461–466.

55 H. Li, K. Cao, J. Cui, S. Liu, X. Qiao, Y. Shen and M. Wang, *Nanoscale*, 2016, **8**, 6379–6385.

56 Q. Luo, H. Ma, Y. Zhang, X. Yin, Z. Yao, N. Wang, J. Li, S. Fan, K. Jiang and H. Lin, *J. Mater. Chem. A*, 2016, **4**, 5569–5577.

57 Z. Wei, H. Chen, K. Yan, X. Zheng and S. Yang, *J. Mater. Chem. A*, 2015, **3**, 24226–24231.

58 I. Jeon, T. Chiba, C. Delacou, Y. Guo, A. Kaskela, O. Reynaud, E. I. Kauppinen, S. Maruyama and Y. Matsuo, *Nano Lett.*, 2015, **15**, 6665–6671.

59 R. Li, X. Xiang, X. Tong, J. Zou and Q. Li, *Adv. Mater.*, 2015, **27**, 3831–3835.

TOC

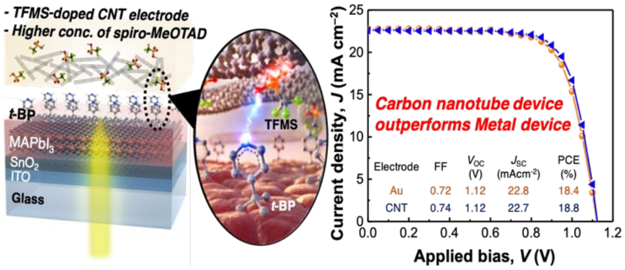
- TFMS-doped CNT electrode
- Higher conc. of spiro-MeOTAD
t-BP
MAPbI$_3$
SnO$_2$
ITO
Glass
TFMS
t-BP
Carbon nanotube device outperforms Metal device
Current density, J (mA cm^{-2})
Applied bias, V (V)
0.0 0.2 0.4 0.6 0.8 1.0 1.2
0 5 10 15 20 25
Electrode FF V_{OC} (V) J_{SC} (mAcm^{-2}) PCE (%)
Au 0.72 1.12 22.8 18.4
CNT 0.74 1.12 22.7 18.8